Metals and Materials International (2023) 29:2385–2397
https://doi.org/10.1007/s12540-022-01364-9

Computational Analysis of the Mechanical Properties of Ta/Cu Nanocomposite Dental Implants: On the Role of Incoherent Interfaces

Arash Kardani[1] · Abbas Montazeri[1] · Herbert M. Urbassek[2,3]

Received: 3 October 2022 / Accepted: 8 December 2022 / Published online: 7 January 2023

Abstract
In recent years, tantalum (Ta)-based nanostructured dental implants have been widely utilized considering their exceptional biocompatibility, bioactivity, and biomechanical properties. Despite their advantages, the mechanical properties of Ta are higher than those of the adjacent jawbone, weakening the bone structure. It has been demonstrated that soft antibacterial additives such as copper (Cu) nanoparticles can tune the mechanical features of Ta-based implants to be similar to those of the adjacent bone. However, a noticeable gap in this research area is the lack of a computational model to explore the interfacial load transfer through the curved interfaces of Ta/Cu nanocomposites. Accordingly, a series of molecular dynamics simulations is employed to survey the microstructural evolution in Ta/Cu nanocomposites subjected to the uniaxial tensile loading condition at the body temperature. Additionally, to provide a complete picture of the contribution of Cu nanoparticles to the results, the mechanisms governing the plastic deformation of nanocomposite models with fine-grained and coarse-grained Ta matrix is systematically examined during the process. In summary, this work provides a comprehensive molecular dynamics simulation of the role of dislocation networks, twin formation, and their mutual interactions on the extent of the plastic zone in various Ta/Cu nanocomposite models.

Keywords Ta/Cu nanocomposite · Dental implants · Molecular dynamics simulation · Uniaxial tension · Curved interface · Plastic deformation mechanisms

1 Introduction

Recently, nanostructured metal-based dental implants have been widely utilized in the medical industry due to their excellent biocompatibility, bioactivity, and biomechanical properties [1, 2]. This is attributed to their outstanding active surface area, which promotes bio-integration and bone ingrowth after implantation [3–5]. In this context, nanostructured tantalum (Ta)-based dental implants have been a focal point of research considering their exceptional biomechanical properties such as high resistance to tensile and compressive stresses, wear, and corrosion [6–8]. As biological and clinical studies emphasized, Ta-based implants have demonstrated the fastest bone cell adhesion rate compared to other candidate materials in this research area, which can reduce the treatment period for patients [9, 10]. Despite its advantages, the application of the pristine tantalum for dental implant purposes is often faced with several issues concerning its mechanical features. Among these, two significant challenges have repeatedly been discussed in the literature. First, the elastic modulus and yield strength of Ta are higher than those of the adjacent bones, which is undesirable based on Wolff's law [11]. It is noted that according to this rule, the human bone gradually adapts itself to the loads to which it is subjected [12]. Therefore, in the case of implants having superior mechanical characteristics compared to the adjacent bones, the implant will remove load from the bone leading to the reduction of bone density over time. The second challenge arises from the difference in the deformation of implant and jawbone under the same imposed stresses, which causes implant loosening through the creation of voids at the implant/bone interface [13].

✉ Herbert M. Urbassek
urbassek@rhrk.uni-kl.de

[1] Computational Nanomaterials Lab (CNL), Faculty of Materials Science and Engineering, K. N. Toosi University of Technology, Tehran, Iran

[2] Physics Department, University Kaiserslautern, Erwin-Schrödinger-Straße, 67663 Kaiserslautern, Germany

[3] Research Center OPTIMAS, University Kaiserslautern, Erwin-Schrödinger-Straße, 67663 Kaiserslautern, Germany

In the literature, two different strategies have been introduced to resolve this issue and to bring the mechanical properties of Ta dental implants closer to those of the adjacent bone. The first strategy consists in creating volumetric and surface porosities within the implant structure to tune its density, elastic modulus, and yield strength, as was thoroughly discussed in [14–16]. The second strategy is to add antibacterial agents with a soft nature such as Cu and Ag to the matrix to make a reduction in its mechanical properties and reinforce the antibacterial features [6, 17–19]. Each of these two routines has its advantages and drawbacks from the materials science point of view that are crucial factors in producing such medical implants. For example, in the case of porous implants, although nanosized pores can accelerate bone cell reproduction, implant cracking is always risky under functional and parafunctional loadings [20–22]. On the other hand, as two antibacterial agents, copper and silver can effectively destroy the bacterial cell walls by the release of ions, which can dramatically decline the post-operation inflammation [17, 23, 24]. However, the deteriorating effects of these additives on the mechanical characteristics of the base Ta, such as the formation of voids at the matrix/interface and softening mechanisms, are not yet fully understood.

An important issue regarding the design of these two-phase load-bearing implants is the load transfer from the matrix to the agent phase, which determines the strength of nanocomposite (NC) implants [25, 26]. It is worth noting that from the biomedical viewpoint, any deformation in the implant during service conditions leads to soft-tissue injuries [2]. Therefore, the characterization of the introduced implants from the point of view of their mechanical properties constitutes is an important issue that should be deeply analyzed. Previous studies have revealed that the elastic properties of metal-matrix NCs strongly depend on the density of disordered atoms located at the grain boundaries (GBs) and interfacial regions [27, 28]. Also, these two regions have been considered as the main sources for the nucleation of dislocations and twins, and thus as the most crucial factors determining the plastic deformation of the introduced NC materials [29, 30]. To comprehend the underlying deformation mechanisms, the microstructural evolution of the crystalline structure of the designed implants should be atomically monitored at different strain levels during the imposed loadings. Experimental-based techniques encounter several limitations on the precise control and measurement at the atomic scale, thus encouraging us to analyze them computationally. Regarding this issue, molecular dynamics (MD) simulation could be successfully utilized to provide a molecular-level picture of the atomic-scale phenomena occurring in these nanostructured materials [31].

Previous numerical investigations have shown that the interfacial area is one of the most critical sites for dislocation nucleation and, therefore, can noticeably affect the mechanical behavior of nanocomposites [32–34]. Carrying out MD simulations, Chen et al. [35], showed that Ta/Cu interfaces play the main role in weakening or strengthening their multilayered systems. They calculated the interface energy in various types of Ta/Cu interfaces, leading to a relationship between this parameter and the dislocation density at the interface area. Their results classified the Ta/Cu interfacial region with respect to their ability to dislocation nucleation and twin formation. Regarding this issue, the HRTEM observations of Zhou et al. [36] demonstrated that the low interface shear resistance in Ta/Cu multilayered nanofilms would enhance dislocation activities in these nanostructures. It is noted that most MD studies on matrix/reinforcement interfaces are devoted to the characterization of planar interfaces, namely the interface of two materials having specified orientations. In the case of the present NC samples, however, the Cu nanoparticle (NP) creates a curved interface in contact with the randomly orientated Ta grains. In this context, Zhang et al. [37, 38] addressed the role of a curved interface on the plastic deformation and fracture mechanisms of bimodal nanotwinned Cu with a composite structure. They observed the emission of first partial dislocations from the curved interface into the NP at small strains. As Wang et al. [39] discussed, a curved interface should be considered as a critical region in terms of stress concentration, making it the main source of defect nucleation. Similarly, the effects of a curved interface and Cu NP deformation on the plastic deformation of a polycrystalline Ta matrix embedded with Cu nanoparticles need to be discussed.

Another crucial factor affecting the deformation mechanisms of Ta/Cu NCs is given by the matrix grain size. The well-known Hall–Petch relationship accurately describes the effect of grain size on the mechanical properties of polycrystalline materials [40, 41]. According to this relation, the strength of polycrystalline metals increases upon decreasing grain size up to a critical value. This arises because GBs hinder the movement of dislocations as the main source of any plastic activity induced within the sample. Below the critical limit, the mentioned plastic deformation is no longer dominated by dislocation motion but is instead a consequence of GB sliding, leading to a decline in strength [42]. Previous studies have addressed this issue for the polycrystalline Ta samples [43–46]. It has been shown that the plastic deformation of coarse-grained polycrystalline Ta occurs mainly through twinning. In contrast, GB-based mechanisms are responsible for the plastic deformation of fine-grained samples. However, the influence of the matrix grain size on the load transfer from the Ta matrix to the Cu NP has not been addressed in the literature up to now.

In the present study, we aim to understand the mechanical behavior and deformation mechanisms of Ta/Cu antibacterial dental implants using MD simulations. It is worth mentioning that most of the published articles in this field

have been devoted to multilayered nanocomposites with flat interfaces. While there is a lack of information concerning antibacterial nanocomposites with curved interfaces. To provide a clear picture of the deformation process affected by the Hall–Petch relationship, we considered several Ta matrix models having various grain sizes infused with one Cu NP of a fixed diameter. An essential preliminary question at this point is the following: How does the presence of the second phase influence the mechanical properties of the Ta-based implants? It has been well established that based on the atomic mismatch between the Ta and Cu atoms, and the different crystalline structures, an incoherent interface is expected to form. Since the load transfer from the matrix to the embedded second phase is noticeably influenced by the degree of interfacial coherency, this issue should be analyzed for the Ta/Cu samples in the present research. Accordingly, we employ a series of MD-based uniaxial tensile tests of these dental NCs at the body temperature (i.e., 310 K) to explore the role of this factor on the nucleation of Shockley partial dislocations, the formation of stacking-fault regions, and the occurrence of twinning in these load-bearing implants. Additionally, to better understand the copper NP contribution to the results, the microstructural evolution occurring of the NC samples with a fine-grained and a coarse-grained Ta matrix is systematically examined during the whole plastic deformation process.

2 Methodology and Simulation Details

2.1 Sample Construction

All Ta/Cu nanocomposite samples were constructed in three steps: first, a cubic polycrystalline Ta sample with the dimensions of 30 × 30 × 30 nm was built as a matrix. Then, a spherical hole was created in the center of the matrix to accommodate the Cu NP. Finally, the Cu phase has filled the central void to resemble the NC sample. All the steps mentioned are schematically shown in Fig. 1 for the NC case with an average grain size of 8 nm. Concerning the antibacterial property of copper inclusion, selecting the optimum concentration of copper NPs would be crucial to make the simulations more applicable. In this context, as discussed in the literature [6, 18, 47, 48], adding 5 wt% Cu to polycrystalline Ta and Ti dental implants decreases the bacteria count impressively. Accordingly, the copper NP with a radius of 8.31 nm and volume fraction (VF) of 8.9%, which corresponds to the mentioned weight percent, was considered as the second phase to make an antibacterial Ta/Cu NC sample. To probe the grain size-dependent structural evolutions of the NC models, keeping the radius of Cu NP fixed, the average grain size of Ta matrix was changed using the Voronoi tessellation method [49, 50]. As such, 9 Ta/Cu NC samples

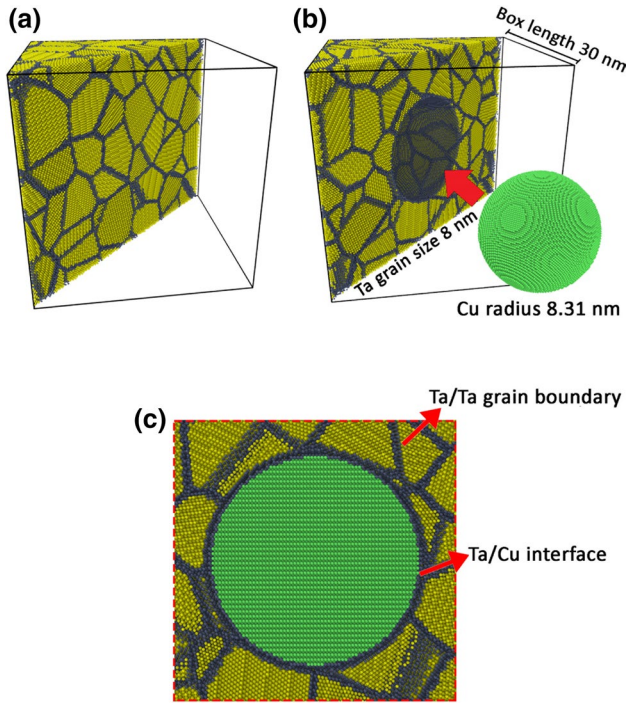

Fig. 1 NC sample construction: **a** building the polycrystalline Ta matrix. **b** Importing the Cu NP. **c** Ta/Cu interface and Ta GBs

Table 1 Geometrical characteristics of the constructed NC samples

Sample	Dimensions (nm^3)	Average Ta grain size (nm)	Number of Ta grains	Total number of atoms
S1	30×30×30	10	50	1,504,031
S2	30×30×30	9	67	1,498,776
S3	30×30×30	8	95	1,492,601
S4	30×30×30	7	141	1,484,145
S5	30×30×30	6	210	1,474,113
S6	30×30×30	5	364	1,457,989
S7	30×30×30	4	670	1,437,652
S8	30×30×30	3	1414	1,402,313
S9	30×30×30	2	1681	1,343,487

having various average grain sizes in the range of 2–10 nm embedded with a Cu NP of constant radius (i.e., 8.31 nm) were constructed as listed in Table 1.

2.2 Details of MD Simulation

Simulations were performed using the open-source LAMMPS code [51]. In line with the previous studies focusing on the mechanical features of Ta/Cu nanostructured samples [35, 52, 53], the Angular-Dependent Potential (ADP) was employed to model the interatomic interactions between

Ta–Ta, Cu–Cu, and Ta–Cu atoms. This potential function considers three angular-dependent terms in addition to the standard form of the well-known EAM potential, which increases the accuracy of the simulations. As thoroughly discussed by Pun et al. [54], the ADP could appropriately model the mechanical and physical characteristics of Ta (BCC), Cu (FCC), and Ta/Cu polycrystalline structures. They calculated lattice constant, cohesive energy, elastic constants, FCC stacking fault energies, surface energies, and phonon frequencies for each phase and compared them to the EAM potential and Ab initio data. It has been demonstrated that more accurate outcomes can be obtained utilizing the ADP at a more reasonable computational cost. Initial velocities were sampled from a Maxwell–Boltzmann distribution at the given temperature. For simulating the evolution of systems in time, the velocity-Verlet integration algorithm with a time-step of 1 fs was chosen [55]. Periodic boundary conditions were assigned to all directions. Also, the Nosé–Hoover thermostat was used to control the simulation temperature.

Before starting any mechanical test, the samples should be in an equilibrium state from the thermodynamics point of view. Hybrid ensembles were implemented here to energetically equilibrate the initial models concerning the complicated structure of the polycrystalline NC samples, including the GB regions and interface areas. For this purpose, first, the samples were geometrically optimized by employing the conjugate gradient (CG) algorithm to prevent atomic overlapping in the regions mentioned. A multi-stage annealing process followed this to achieve a fully relaxed structure before stretching. To this end, first, each sample was relaxed at 310 K for 200 ps. In the next step, further high-temperature annealing was applied at 1086 K (i.e., 80% of the melting temperature of copper) for 200 ps to guarantee the stability of GBs, as discussed in detail in Ref. [56]. The process was terminated by cooling the sample to experience the final annealing at 310 K for 200 ps. To keep the pressure fixed at zero in all directions during the equilibration, an isothermal-isobaric (NPT) ensemble was implemented. To further analyze the hybrid relaxation method, the interface region was thoroughly examined to ensure the lack of dislocations or atomic overlap before applying the uniaxial tension. Figure 2 displays the interfacial area at the end of the equilibration, demonstrating no sign of dislocation creation at the interface. Additionally, we found a reduction in the Ta/Cu interface energy after the annealing process from -71.88 to -72.13 J/m^2, showing the stability of the interfacial area after the proposed relaxation scheme. To apply the uniaxial elongation, all samples were stretched at a strain rate of 5×10^8 s^{-1} along the two opposite sides of the simulation box in the axial direction [44, 57, 58]. The deformation proceeded until the strain level of 40%. It is worth mentioning that during the uniaxial tensile test, the pressure was kept constant at zero in both lateral directions.

2.3 Crystal Structure Analysis Tools

In this study, the OVITO software package was implemented to visualize the microstructure of NC samples [59]. Dislocations and stacking faults were identified using the dislocation extraction analysis (DXA) developed by Stukowski et al. [60]. Polyhedral Template Matching (PTM) was employed to classify the local crystalline structure of atoms. This

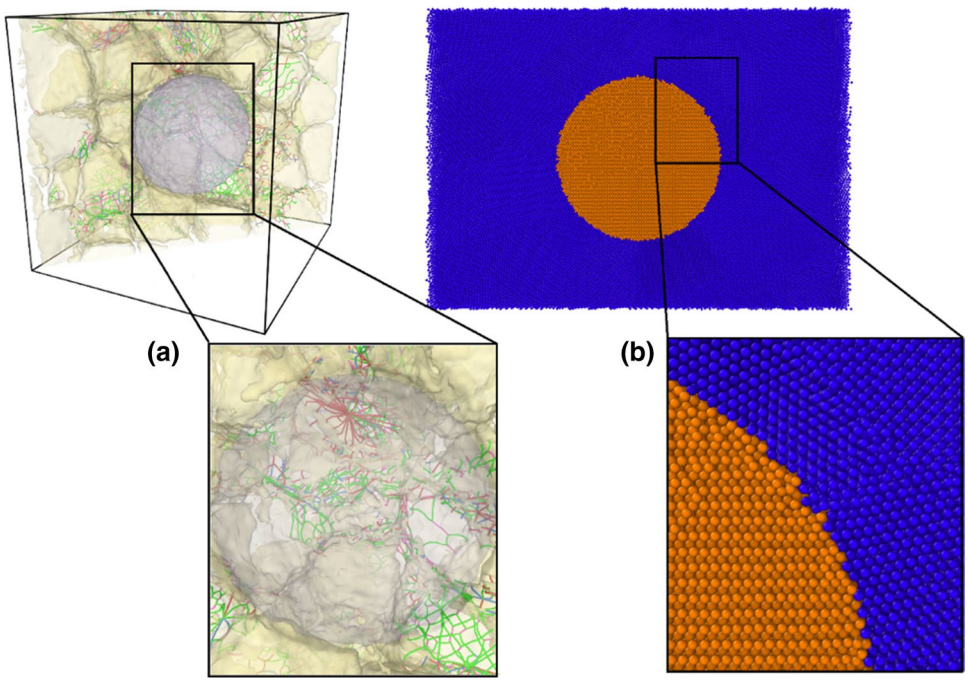

Fig. 2 Stable Ta/Cu interface after relaxation: **a** dislocation-free interface and **b** lack of atom overlap

approach directly calculates the local crystal orientation at the GBs, interfaces, and other disordered regions. Therefore, it can be a powerful tool for detecting stacking fault regions and distinguishing twinned and untwinned areas [61]. We also utilized the von-Mises stress distribution map to determine the stress concentration at the GBs, Ta/Cu interface, and grain interiors. Additionally, this tool was used to characterize the contribution of each grain in the plastic deformation of the whole NC sample having coarse-grained and fine-grained matrices.

3 Results and Discussion

3.1 Grain-size Dependent Mechanical Properties of the NC Models

Figure 3 shows the stress–strain diagrams of the NC samples with different matrix grain sizes. As seen, yield and maximum stress values decrease with grain size reduction. After passing the maximum stress in the plastic area, the curve enters the steady-state region displaying a strain-independent behavior. As Pande et al. [62] discussed, the stress variations in this zone are entirely associated with plastic deformation, which can be thoroughly analyzed by probing the evolution of structural defects within the stretched samples. Variations of the elastic modulus and flow stress of the NC models with the average grain size of the Ta matrix have been plotted in Figs. 4 and 5, respectively. Here, the former was directly computed as the initial slope of the stress–strain curve in the elastic region (i.e., $\varepsilon < 2\%$). Additionally, the average of the stress values in the strain range of 0.2–0.4 has been considered as the flow stress. To better understand the role of the additive Cu phase, these data have also been provided for the pure Ta samples having the same geometrical characteristics [63].

As seen, the presence of the Cu NP as a softer material decreases the elastic resistance of the base Ta matrix. It is also revealed that there is a direct correlation between the

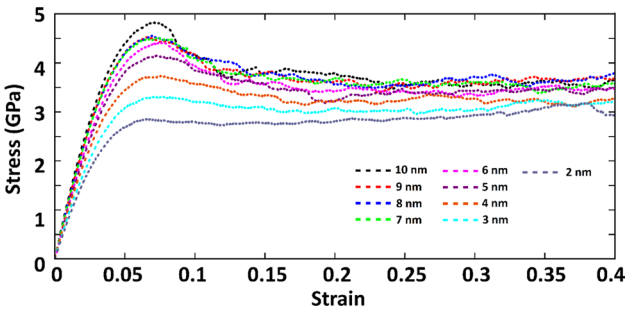

Fig. 3 Stress–strain diagram of Ta/Cu NC samples with various grain sizes under tension at 310 K

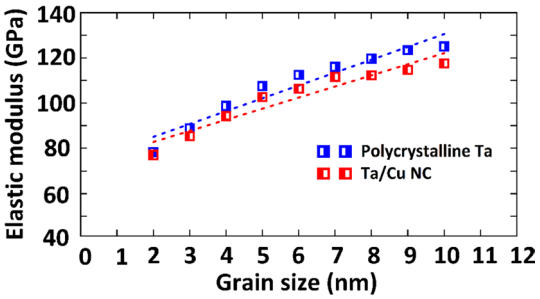

Fig. 4 Variation of the elastic modulus of NC and pure Ta samples with the average grain size of the Ta matrix at 310 K

elastic modulus of the NC samples and the average grain size of the Ta matrix. It arises because the elastic modulus of the GB areas is smaller than that of the grain interiors [64–66]. This is attributed to the higher amount of potential energy of the GB atoms originating from larger atomic misalignment in these regions. To examine this issue for the present samples, the grain and GB regions have been distinguished based on their potential energy for the sample with an average grain size of 8 nm (see Fig. 6a). As seen, the GB areas have higher potential energy in comparison with the grain interiors. Consequently, as depicted in Fig. 6b, with increasing grain size, the contribution of GB atoms decreases, leading to the observed modulus enhancement in the coarse-grained structure of polycrystalline NC samples. To further analyze this issue, we plotted the elastic modulus against the relative density for the NC samples with different grain sizes listed in Table 1. As seen in Fig. 7, this elastic constant decreases linearly with decreasing the overall density of the NC models, which is attributed to the increased fraction of GB atoms in fine-grained samples. A similar trend has been reported by Pan et al. [43] for the correlation between the elastic modulus and relative density of polycrystalline Ta samples, demonstrating the accuracy of our results. Concerning the flow stress curves, it was deduced that the Cu component could influence not only the elastic resistance,

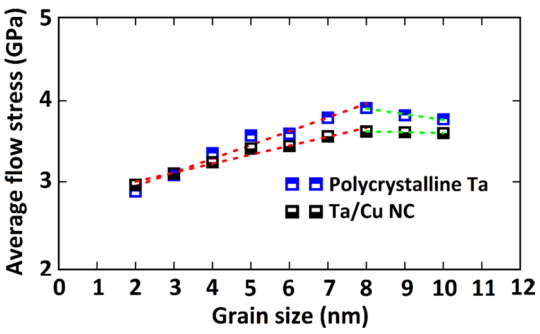

Fig. 5 Comparison of the obtained flow stress for Ta–Cu NC samples having various grain sizes at 310 K with those obtained for pure Ta samples

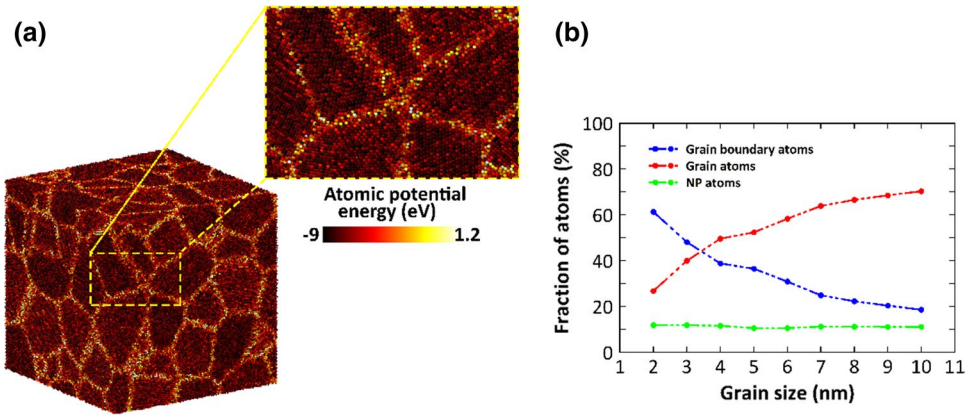

Fig. 6 **a** Analysis of the atomic potential energy for the sample with an average grain size of 8 nm and **b** dependence of the fraction of GB atoms on the matrix grain size

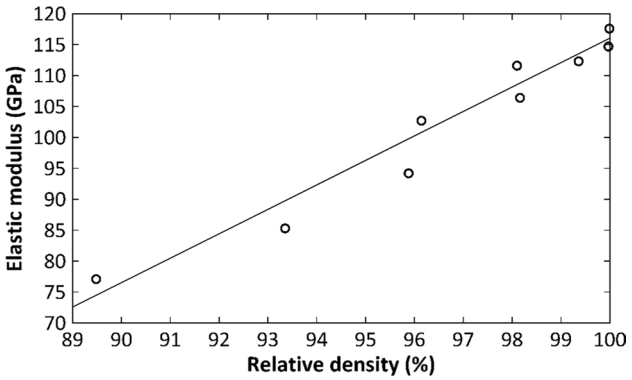

Fig. 7 Variation of elastic modulus of NC models listed in Table 1 versus their overall density

but also the plastic one. Another critical point is the convergence of the results in the samples with smaller grain sizes, which will be deeply analyzed in Sect. 3.3.

3.2 Microstructural Characterization of the Interfacial Area

As previously mentioned, to comprehensively explore the mechanisms governing the plastic deformation of Ta/Cu NCs, it is necessary to characterize the microstructural evolution of the interfacial region. In two-phase metallic systems with different crystallographic structures, the formation of an incoherent interface is a common phenomenon [67]. As Zhang et al. [68] reported, flat fcc/bcc incoherent interfaces could act as favorite sites for dislocation nucleation owing to their lower energetic barriers. In contrast, these regions have been demonstrated to block the transition of dislocations from one phase to the other, enhancing the strength of composite structures [69]. It is worth mentioning that this issue has rarely been considered in the literature for curved interfaces such as the one studied in the present work. Accordingly, to capture the mechanisms dominating the deformation of Ta/Cu NC samples, evolution of the dislocations and stacking faults was thoroughly studied utilizing the DXA method. Figure 8a–e represent the DXA results for the Ta/Cu NC sample with 8 nm grain size at various strain levels.

As depicted in this figure, the nucleation of partial dislocations and stacking faults started from the interface region towards the copper NP. This was followed by the emission of new dislocations and twins with increasing imposed strain. This is attributed to the local high-stress points at the interfacial region, facilitating defect nucleation in the copper side due to its lower activation barrier. Similarly, carrying out MD simulations for Cu-Ta interfaces, Heino [70] noticed that defect formation and failure occur most often in the Cu phase. Figure 8f supports the outcomes by detecting stress concentration in the interfacial region and GBs. In addition to the bcc/fcc incoherent interface, the stress concentration was also influenced by the softer nature of Cu compared to the Ta phase. In this context, Rajput et al. [32] studied Al/Ti and Al/Mg NC systems with fcc/hcp incoherent interfaces in terms of stress concentration and deformation mechanisms. They found that the lower elastic modulus of Mg would increase the stress concentration in the interface. Moreover, it was revealed that the lack of dislocation activity promotes the formation of voids, facilitating the NC failure. Contrary to this study, the current work deals with the Cu inclusion having fcc structure, which is susceptible to plastic deformation by dislocations and twins. Based on the above discussion, the Ta/Cu incoherent interface is expected to enhance the chance of defect formation inside the spherical copper NP.

To support these findings, the defect-based microstructural evolution of the copper NP embedded within the NC sample having an average grain size of 8 nm is illustrated in Fig. 9 at various strains. As depicted in Fig. 9a, the first Shockley partial dislocations were nucleated exactly from the interface region. Accordingly, the Ta/Cu interface could be considered the main source of dislocation formation. As disclosed in Fig. 9b, stacking fault (SF) planes were then extended between two Shockley partial dislocations at the

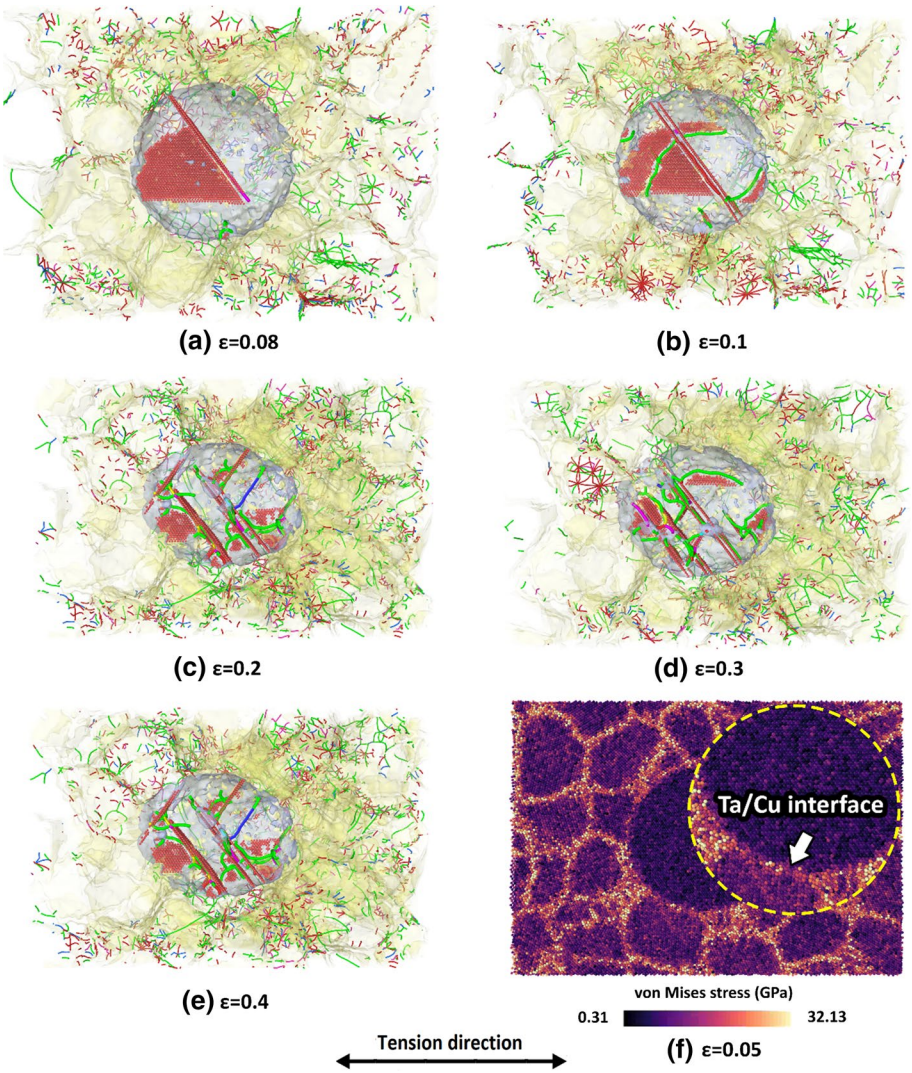

Fig. 8 Cross-section of Ta/Cu NC sample with 8 nm grain size at various strains: **a**–**e** DXA analysis results, **f** von Mises stress map

strain of 0.1. The first twin boundaries were also detected at this strain level. As thoroughly discussed in the literature, the formation of such twins in copper can be divided into three steps [12–14]. Initially, intrinsic stacking faults are formed between two Shockley partial dislocations. This is followed by converting intrinsic stacking faults to extrinsic ones by placing an atomic layer between the two HCP planes. Finally, expansion of extrinsic stacking faults by adding the other atom layers leads to the appearance of twinned areas distinguished by sharp twin boundaries. Therefore, it can be deduced that the formation and expansion of stacking faults can be enumerated as two main prerequisites of twin formation in the copper phase. It is noted that dislocation nucleation occurred continuously during the deformation process, increasing the dislocation density. This phenomenon promoted the formation of lock dislocations shown in Fig. 9c, in which yellow and pink vectors denote the Burgers vector of Hirth and stair-rod dislocations, respectively. By further straining, some perfect dislocations were dissociated into partial ones (Fig. 9d) owing to the low stacking fault energy (SFE) of Cu, which enhanced the stacking fault density. As an example, the observed perfect dislocation dissociation at point P in Fig. 9d can be represented as:

$$\frac{1}{2}\langle 0\bar{1}\bar{1}\rangle \rightarrow \frac{1}{6}\langle \bar{1}\bar{2}\bar{1}\rangle + \frac{1}{6}\langle 1\bar{1}\bar{2}\rangle .$$

As discussed earlier, the dislocations in the copper NP are mostly identified as Shockley partials. Considering the intrinsic stacking fault induced by these dislocations, the SF planes would be expected to act as an obstacle in the slip path of dislocations due to changing the FCC structure to HCP. It has been demonstrated that SFs can increase the strain hardening of materials by interrupting the dislocations slip [71]. On the other hand, the mobile nature of Shockley partial dislocations increases the number of other slip barriers during the deformation. Figure 9e, f show the formation of stair-rod and Hirth dislocations originating from partial-dislocation interactions. For example, at point "Sr"

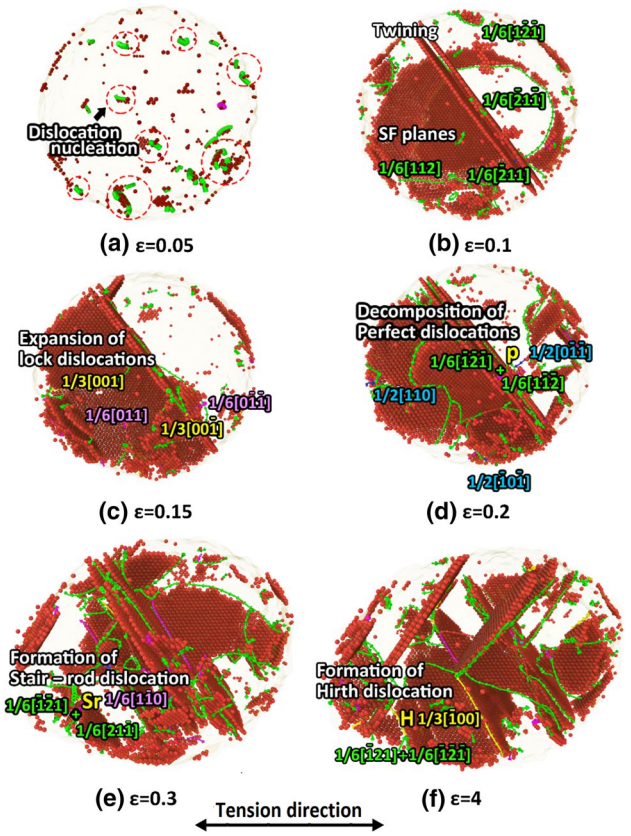

Fig. 9 Dislocations in the Cu NP of the Ta/Cu NC sample with an average grain size of 8 nm at various strain levels

in Fig. 9e, two partial dislocations combined as stated in the following equation to form a stair-rod dislocation having a sessile nature:

$$\frac{1}{6}\langle\bar{1}\bar{2}1\rangle + \frac{1}{6}\langle 21\bar{1}\rangle \rightarrow \frac{1}{6}\langle 1\bar{1}0\rangle .$$

Similarly, as seen in Fig. 9f, by increasing the strain level, two Shockley partial dislocations interact to form a Hirth lock dislocation based on the following reaction:

$$\frac{1}{6}\langle\bar{1}21\rangle + \frac{1}{6}\langle\bar{1}\bar{2}\bar{1}\rangle \rightarrow \frac{1}{3}\langle\bar{1}00\rangle .$$

It is noted that all mentioned dislocation reactions are energetically favorable in terms of the Frank rule. Also, since the sliding direction of Hirth and stair-rod dislocations do not correspond to close-packed directions [16], they remained stable, acting as obstacles for the other dislocations during the process. Therefore, they could successfully limit the slip of their mobile counterparts. As such, the soft Cu NP sample faces a complex deformation and does not deform faster than the hard Ta matrix during the deformation of the NC sample.

Similarly, in the research conducted by Mishra et al. [17] to explore the dislocation interaction effects on the plastic deformation of high-entropy alloy-coated single-crystal Cu substrate during the nanoindentation, it was demonstrated that the dislocation entanglements resulting from the formation of lock dislocations lead to the strain hardening and forest hardening phenomena. Concerning previous studies [32, 38, 72], non-uniform deformation between the matrix and second phase is an essential factor in the interface's void formation, which leads to the NC failure during loading. In the case of the present NC sample, however, no void was detected in the interfacial region. As previously mentioned, this arises because the SF planes and lock dislocations would inhibit the dislocation slip during the deformation, which can effectively control the deformation rate in the copper NP.

3.3 Unraveling the Governing Deformation Mechanisms

Based on the obtained results, the Ta/Cu interface demonstrated a crucial role in the formation of dislocations during the loading process of NC models. Moreover, it was revealed that Shockley partial dislocations with SF planes are the most common defects in the introduced samples. We also found that Shockley partial interactions would affect the mechanical features of the Cu phase via the creation of lock dislocations. In this context, the effect of twinning formation on the stacking fault evolutions is a vital question that should be answered for further achievements in this research topic. Targeting this purpose, the twinning evolutions were also monitored for the introduced Ta/Cu NC sample at different strain levels. Figure 10 displays the corresponding PTM analysis data, in which yellow and black dashed circles reveal the nucleation of SFs from the interface and twin boundary areas, respectively.

According to Fig. 10a, there is no sign of SF planes or twins at the strain of 0.05, showing that the stress was insufficient to nucleate defects at the interface. As depicted in Fig. 10b, with increasing the imposed strain, intrinsic stacking faults are observed in the interface area, which are expanded through the Cu NP (see SF1-SF4). Also, it can be seen that the mutual interaction of the SF1 and SF2 limits their further growth. As discussed before, twins are responsible for the plastic deformation of the matrix grains. Similarly, twinning is also favorable in the copper phase [73]. However, there is an essential difference between the nature of twins in the Ta and Cu phases, which can be understood by probing the nucleation process of each phase. In the case of the Ta matrix, twins are directly nucleated from the GB areas. In contrast, twins in the copper side can be formed from SF planes. As mentioned before, this phenomenon is initiated by creating

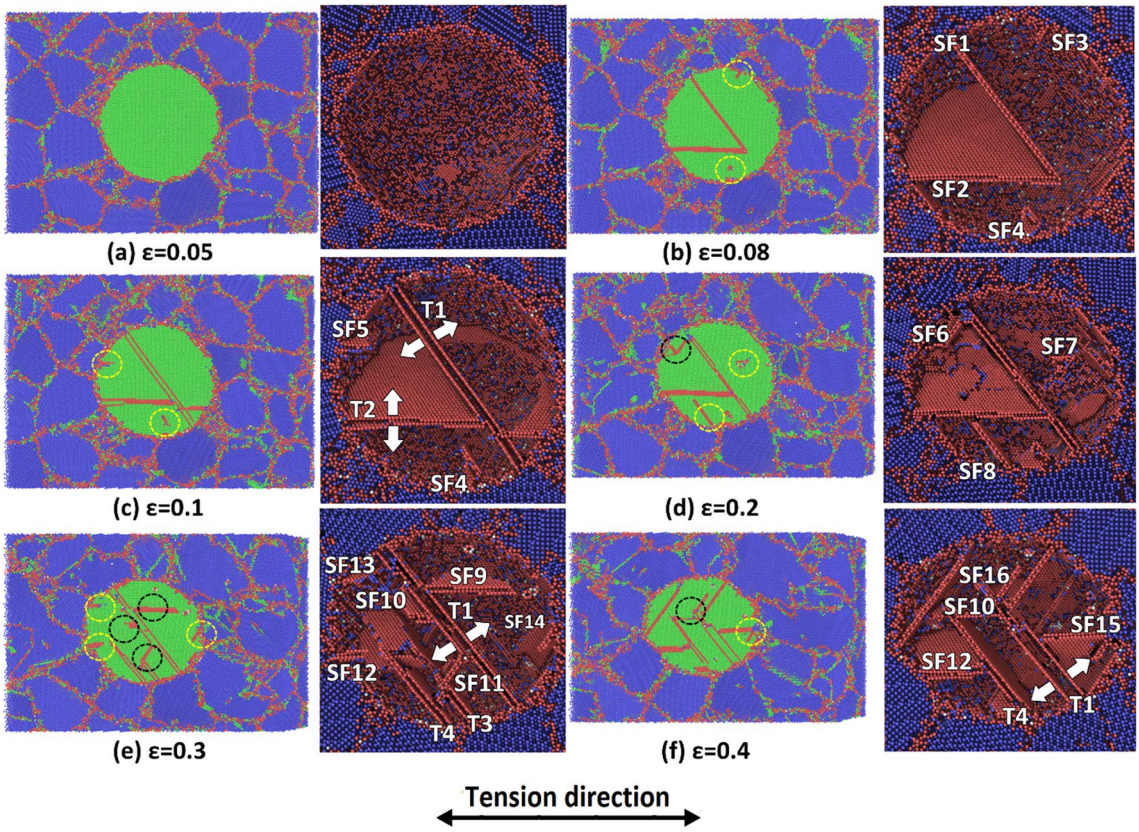

Fig. 10 PTM analysis results for the Ta/Cu NC sample with an average grain size of 8 nm: **a**–**f** display the formation and mutual interaction of stacking faults and twins at various strain levels

intrinsic SFs between two partial dislocations. The intrinsic SFs will then convert to extrinsic ones, forming twin boundaries within the Cu nanoparticle.

As seen in Fig. 10c, the two intrinsic stacking faults created in the previous strain (see SF1 & SF2 in Fig. 10b) altered into the extrinsic ones to form twins (see T1 & T2). As the white arrows show, both of these twins got thicker during the process. While Ta/Cu interface was considered the main factor of SFs nucleation, our results show that twin boundaries play a crucial role in the SFs nucleation. As black dashed circles indicate in Fig. 10d–f, new intrinsic SFs were nucleated from the twin boundaries (see SF6, SF9–SF11, and SF16). Such results provide sufficient evidence demonstrating that twin boundaries of the copper phase are the other sources of defect nucleation at high strain levels, which is also in good agreement with the data reported by Zhang et al. [38] in the case of Cu/Cu NC sample. The main similarities are as follows:

- Only in the case of low twin density, defects can be nucleated from the twins.
- Defects nucleation from the twin boundaries occurs at strains of more than 15%.
- This phenomenon depends on the angle between the twin and load direction and can be seen at all angles except 45°.

It is worth mentioning that in addition to the formation of SFs, twins, and dislocations, the plastic deformation of metals is also under the influence of twin-dislocation and twin-twin interactions [74, 75]. In the present study, with increasing the density of twins, the new nucleated SFs lose the chance of expansion due to being blocked by other twins. For example, SF11, nucleated from T1 twin boundary, was blocked by T3 during the expansion process (Fig. 10e). On the other hand, by enhancing the applied strain from 0.3 to 0.4, T4 suddenly grew and stopped the expansion of SF10 and SF12. According to these findings, twins can be considered unpredictable obstacles in the growth path of SFs during the deformation process at high strain levels. As such, it can be concluded that the mechanical properties and deformation behavior of coarse-grained Ta/Cu NCs are remarkably affected by the complexity of the plastic deformation in the copper phase. In the case of fine-grained samples, the number of stress-affected grains increases. As a result, the contribution of the copper nanoparticle to the plastic

deformation of the whole NC sample would be expected to decrease.

To further clarify this issue, the microstructural changes of the sample with an average grain size of 4 nm were probed at different strain levels using the PTM analysis (see Fig. 11). As seen in Fig. 11a, b, Cu NP showed a defect-free structure until the strain of 0.08, suggesting the absorption of the stress-induced energy by the GBs of the matrix. It was deduced that the applied stress is distributed over a more significant number of grains by reducing the Ta grain size. Thus, Cu NP remained defect-free. Surprisingly, this phenomenon is entirely different from what was observed for the sample with an average grain size of 8 nm at the same strain level (see Fig. 10b). Snapshots of the SF evolutions provided in Fig. 11c–f show the lower density of SF planes in this case compared to the sample with the average grain size of 8 nm, leading to lower twins-SFs interactions in the copper NP.

Additionally, we found that the chance of twin formation was reduced for the fine-grained matrix since most of the SFs were not stable enough to be converted to extrinsic ones during the plastic deformation. For quantitative comparison, the number of HCP atoms within the Cu NP was calculated for the samples with average grain sizes of 10, 8, and 4 nm at different strains. As illustrated in Fig. 12,

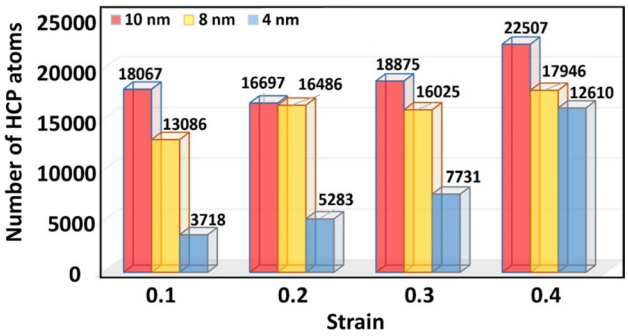

Fig. 12 Comparison of the evolution of the number of HCP atoms with strain in various NC samples

the number of HCP atoms in Cu NP decreased with reducing the Ta grain size at all strain levels. As such, it was concluded that the average grain size of the Ta matrix plays a crucial role in the deformation of the NC sample. To broaden our insight into the role of grains on the plastic deformation of nanocomposite samples, the atomic shear strain distribution maps were compared inside the grains of two Ta/Cu NC samples having average grain sizes of 4 and 8 nm at different values of imposed strain

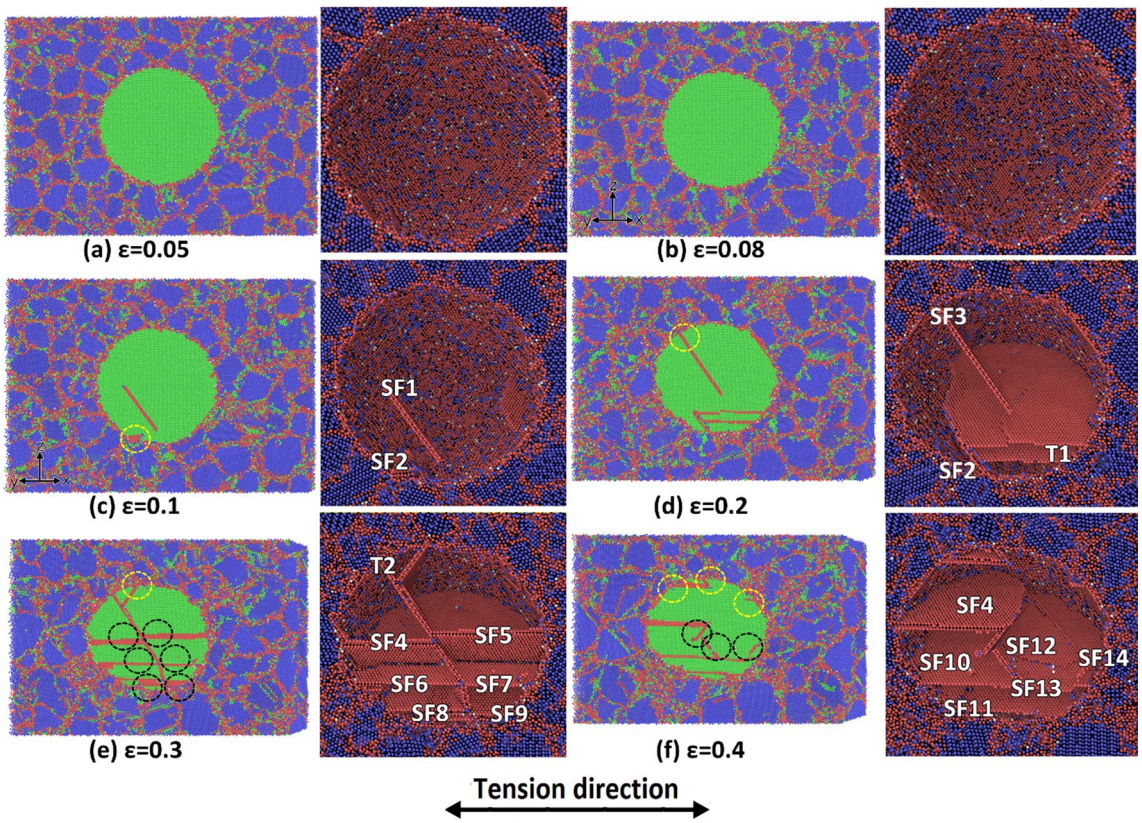

Fig. 11 PTM analysis results for the Ta/Cu NC sample with an average grain size of 4 nm: **a**–**f** display the formation and mutual interaction of stacking faults and twins at various strian levels

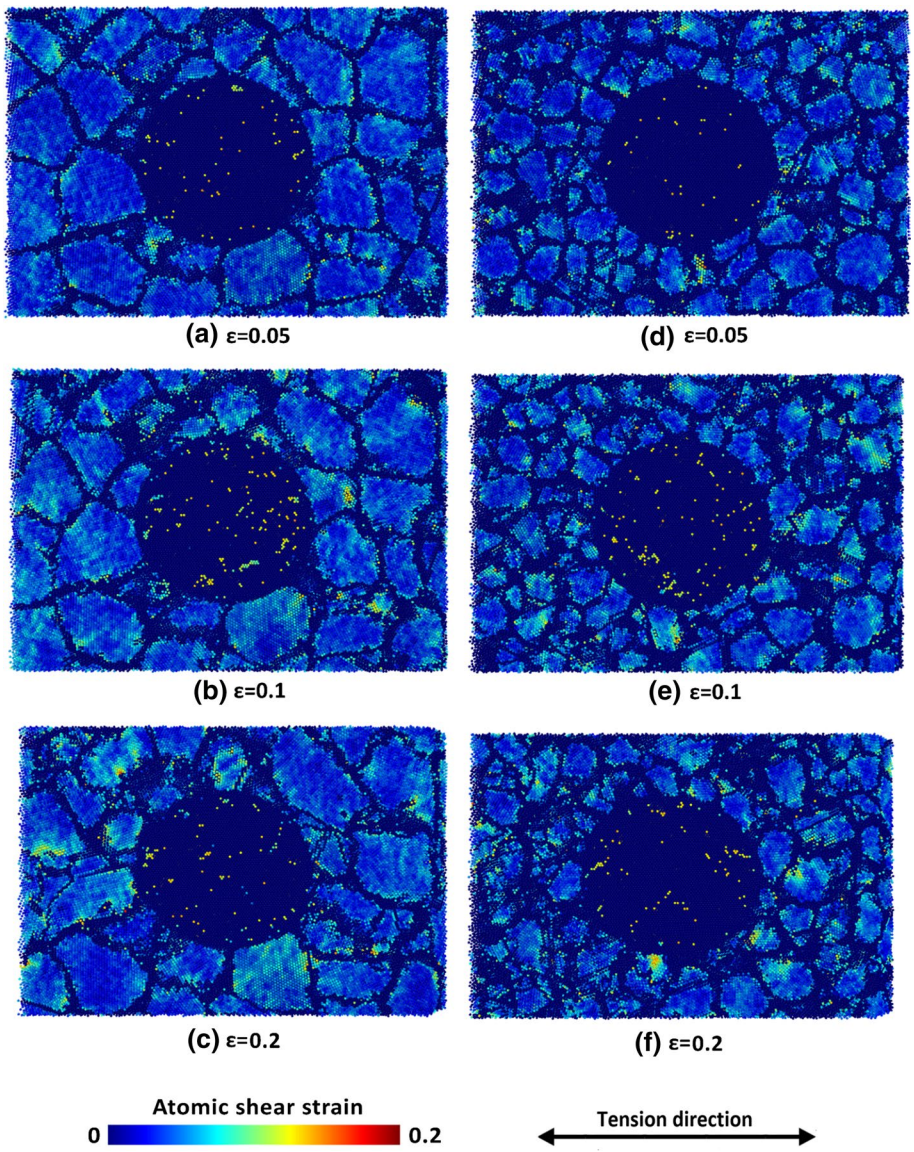

Fig. 13 Atomic shear strain distribution map of matrix grains for the Ta/Cu NC samples at different strain levels: **a**–**c** coarse-grained and **d**–**f** fine-grained NC samples. Dark blue atoms represent the less deformed parts of each grain. In contrast, light blue, green and red atoms show the deformed parts of each grain caused by dislocation slip or twinning activities. (Color figure online)

(see Fig. 13). As seen, for the finer-grained Ta matrix, the mechanical characteristics of the NC model are less affected by the presence of the embedded copper NP. These findings would manifest themselves in the results reported in Fig. 5, in which the flow stress curve of the NC model converges to that of the polycrystalline pure Ta sample by reducing the average grain size of the matrix. It is worthy to note that contrary to what was expected for the ultrafine-grained samples, in which the dominant deformation mechanism switches to the GB sliding, the presence of a Cu NP would not lead to an increase in the flow stress of NC samples compared to the pure Ta model. That was attributed to the softer nature of the Cu NP compared to the Ta matrix and the formation of an incoherent interface in these case studies as thoroughly discussed in the literature [76–78].

4 Conclusion

In the present study, the mechanical characteristics of Ta/Cu nanocomposite dental implants were systematically examined at the body temperature through MD simulation of the uniaxial tensile test. Additionally, several crystal structure analysis tools provided by the OVITO software were employed to get more insight into their plastic deformation mechanisms. To this end, first, grain-size dependent mechanical properties of the NC models were studied. It was deduced that decreasing the grain size would reduce the values of elastic modulus and yield stress. Comparing the results with those of the pure Ta, we found that the presence of Cu NP as a softer material decreases the elastic resistance and average flow stress of the base matrix. To comprehensively explore the underlying mechanisms, the DXA technique was implemented to

characterize the microstructural evolution of the interfacial region and the copper NP. Based on the results obtained for the NC model with an average grain size of 8 nm at various strain levels, nucleation of partial dislocations and stacking faults started from the interface. Upon increasing the strain level, the emission of new dislocations and their expansion from the interfacial region toward the copper NP would be observed, facilitating twin formation in the copper phase. This was attributed to the lower activation barrier of the Cu side in the incoherent fcc/bcc interface and its softer nature compared to the Ta phase. Additionally, we found that defect transmission, which is a common phenomenon in NC systems with a coherent interface, does not occur from the Ta matrix to the Cu NP or vice versa due to the incoherent nature of the interface. It was demonstrated that this phenomenon is independent of the NP size and the average grain size of the Ta matrix. It was also revealed that Shockley partial interactions would affect the mechanical features of the copper NP via the creation of lock dislocations, inhibiting the dislocation slip during the process. As a result, no void formation was observed in the interfacial region of the models, which could successfully postpone the NC failure.

Employing the PTM analysis, we further proceeded to explore the role of twin formation on the stacking fault evolution during the process. For the coarse-grained model having an average grain size of 8 nm, it was shown that twin boundaries of the copper NP play a significant role in the nucleation of SFs at the high strain level conditions. Surprisingly, twins could also be imagined as obstacles in the growth path of SFs, leading to the complicated plasticity induced within the Cu phase. Moreover, microstructural changes of a fine-grained sample with an average grain size of 4 nm were probed to determine the correlation between the Ta average grain size and the contribution of the Cu NP to the plastic deformation of the NC sample. A lower density of SF planes was found in the fine-grained model, which also reduced the chance of twin formation. This was attributed to the distribution of the applied stress over more significant grains in this case. It was demonstrated that reducing the average grain size of the Ta matrix would diminish the role of the embedded Cu phase on the results. Consequently, the flow stress curve of the nanocomposite model converged to that of the pure Ta sample for the ultrafine-grained models. Our research can provide a guideline for designing the geometrical characteristics of Ta/Cu nanocomposites that can be potentially used for the next generation of dental implants.

Acknowledgements We acknowledge support by the Deutsche Forschungsgemeinschaft (DFG, German Research Foundation)—project number 441110175—UR 32/28-1. Simulations were performed at the High Performance Cluster Elwetritsch (RHRK, TU Kaiserslautern, Germany).

Funding Open Access funding enabled and organized by Projekt DEAL.

Data Availability No data was used for the research described in this article.

Declarations

Conflict of interest The authors declare that they have no conflict of interest.

References

1. S. Magesh, G. Vasanth, A. Revathi, M. Geetha, in *Nanobiomaterials*, ed. by R. Narayan (Woodhead Publishing, Cambridge, 2018), pp. 481–501
2. C.E. Misch, *Dental Implant Prosthetics*, 1st edn. (Mosby, Maryland Heights, 2004)
3. E. Bressan, L. Sbricoli, R. Guazzo, I. Tocco, M. Roman, V. Vindigni, E. Stellini, C. Gardin, L. Ferroni, S. Sivolella, B. Zavan, Int. J. Mol. Sci. **14**, 1918–1931 (2013)
4. B.H. Sagherian, R.J. Claridge, Orthop. Clin. N. Am. **50**, 119–129 (2019)
5. R.A. Gittens, R. Olivares-Navarrete, Z. Schwartz, B.D. Boyan, Acta Biomater. **10**, 3363–3371 (2014)
6. J. Cui, L. Zhao, W. Zhu, B. Wang, C. Zhao, L. Fang, F. Ren, J. Mech. Behav. Biomed. Mater. **74**, 315–323 (2017)
7. J. Ma, W. Sun, F. Gao, W. Guo, Y. Wang, Z. Li, Sci. Rep. **6**, 28227 (2016)
8. I. Putrantyo, N. Anilbhai, R. Vanjani, B. De Vega, J. Biomim. Biomater. Biomed. Eng. **52**, 55–65 (2021)
9. C.G. Paganias, G.A. Tsakotos, S.D. Koutsostahis, G.A. Macheras, Curr. Res. Med. **5**, 63–72 (2014)
10. L.-Y. Shi, A. Wang, F.-Z. Zang, J.-X. Wang, X.-W. Pan, H.-J. Chen, Colloid. Surf. B **160**, 22–32 (2017)
11. H.M. Frost, Angle Orthod. **64**, 175–188 (1994)
12. R.L. Sakaguchi, J.M. Powers (ed.), *Craig's Restorative Dental Materials*, 13th edn. (Mosby, Maryland Heights, 2012)
13. M.I.Z. Ridzwan, S. Shuib, A.Y. Hassan, A.A. Shokri, M.N. Mohamad Ibrahim, J. Med. Sci **7**, 460–467 (2007)
14. V.K. Balla, S. Bodhak, S. Bose, A. Bandyopadhyay, Acta Biomater. **6**, 3349–3359 (2010)
15. V.K. Balla, S. Bose, N.M. Davies, A. Bandyopadhyay, JOM **62**, 61–64 (2010)
16. S. Arabnejad, R. Burnett Johnston, J.A. Pura, B. Singh, M. Tanzer, D. Pasini, Acta Biomater. **30**, 345–356 (2016)
17. S. Wang, W. Zhu, P. Yu, X. Wang, T. He, G. Tan, C. Ning, Mater. Technol. **30**, B120–B125 (2015)

18. A.V. Pervikov, E.S. Dvilis, A.P. Khrustalev, O.V. Bakina, V.D. Paygin, A.S. Lozhkomoev, A.V. Chumaevsky, O.L. Khasanov, M.I. Lerner, Inorg. Mater. Appl. Res. **12**, 755–761 (2021)
19. Y. Qing, L. Cheng, R. Li, G. Liu, Y. Zhang, X. Tang, J. Wang, H. Liu, Y. Qin, Int. J. Nanomed. **13**, 3311 (2018)
20. A. Bandyopadhyay, I. Mitra, A. Shivaram, N. Dasgupta, S. Bose, Addit. Manuf. **28**, 259–266 (2019)
21. M.G. Kim, Met. Mater. Int. **17**, 705–711 (2011)
22. A. Smirnov, J.I. Beltrán, T. Rodriguez-Suarez, C. Pecharromán, M.C. Muñoz, J.S. Moya, J.F. Bartolomé, Sci. Rep. **7**, 44922 (2017)
23. J.H. Hsieh, T.H. Yeh, C. Li, C.H. Chiu, C.T. Huang, Vacuum **87**, 160–163 (2013)
24. V.M. Villapún, L.G. Dover, A. Cross, S. González, Materials **9**, 736 (2016)
25. L. Ceschini, A. Dahle, M. Gupta, A.E.W. Jarfors, S. Jayalakshmi, A. Morri, F. Rotundo, S. Toschi, R.A. Singh, in *Aluminum and Magnesium Metal Matrix Nanocomposites*, ed. by L. Ceschini, A. Dahle, M. Gupta, A.E.W. Jarfors, S. Jayalakshmi, A. Morri, F. Rotundo, S. Toschi, R.A. Singh (Springer, Singapore, 2017), pp.1–17
26. A. Kardani, A. Montazeri, Sci. Rep. **10**, 9745 (2020)
27. J. Li, B. Lu, H. Zhou, C. Tian, Y. Xian, G. Hu, R. Xia, Phys. Lett. A **383**, 1922–1928 (2019)
28. Y. Wang, J. Zuo, N. Jiang, K. Niu, Y. Wu, Comput. Mater. Sci. **171**, 109272 (2020)
29. S.L. Thomas, K. Chen, J. Han, P.K. Purohit, D.J. Srolovitz, Nat. Commun. **8**, 1764 (2017)
30. B. Jiang, A. Tu, H. Wang, H. Duan, S. He, H. Ye, K. Du, Acta Mater. **155**, 56–68 (2018)
31. Christopher R. Weinberger, Garritt J. Tucker, *Multiscale Materials Modeling for Nanomechanics* (Springer, Cham, 2016)
32. A. Rajput, S.K. Paul, J. Alloy. Compd. **869**, 159213 (2021)
33. A. Kardani, A. Montazeri, Comput. Mater. Sci. **144**, 223–231 (2018)
34. S. Mohammadi, A. Montazeri, H.M. Urbassek, Wear **444–445**, 203117 (2020)
35. J. Chen, S.N. Mathaudhu, N. Thadhani, A.M. Dongare, Sci. Rep. **10**, 208 (2020)
36. Q. Zhou, J.J. Li, F. Wang, P. Huang, K.W. Xu, T.J. Lu, Scr. Mater. **111**, 123–126 (2016)
37. F. Zhang, J. Zhou, Comput. Mater. Sci. **145**, 60–67 (2018)
38. F. Zhang, Y. Zhi, G. Li, C. Xun, D. Zhu, Appl. Phys. A **127**, 370 (2021)
39. L. Wang, W. Liu, B. Zhu, W. Chen, F. Zhang, B. Liu, J. Liu, J. Zhou, Y. Zhao, J. Mater. Res. Technol. **14**, 2071–2084 (2021)
40. E.N. Hahn, M.A. Meyers, Mater. Sci. Eng. A **646**, 101–134 (2015)
41. N.H. Heo, Y.-U. Heo, S.K. Kwon, N.J. Kim, S.-J. Kim, H.-C. Lee, Met. Mater. Int. **24**, 265–281 (2018)
42. S.N. Naik, S.M. Walley, J. Mater. Sci. **55**, 2661–2681 (2020)
43. Z. Pan, Y. Li, Q. Wei, Acta Mater. **56**, 3470–3480 (2008)
44. C. Huang, X. Peng, Y. Zhao, S. Weng, B. Yang, T. Fu, Mater. Sci. Eng. A **738**, 1–9 (2018)
45. Y. Tang, E.M. Bringa, M.A. Meyers, Mater. Sci. Eng. A **580**, 414–426 (2013)
46. L. Smith, J.A. Zimmerman, L.M. Hale, D. Farkas, Model. Simul. Mater. Sci. Eng. **22**, 045010 (2014)
47. Y. Wu, H. Zhou, Y. Zeng, H. Xie, D. Ma, Z. Wang, H. Liang, Materials (Basel) **15**, 2342 (2022)
48. R. Liu, Z. Ma, S. Kunle Kolawole, L. Zeng, Y. Zhao, L. Ren, K. Yang, J. Mater. Sci. Mater. Med. **30**, 75 (2019)
49. C.H. Rycroft, Chaos Interdiscip. J. Nonlinear Sci. **19**, 041111 (2009)
50. S. Falco, J. Jiang, F. De Cola, N. Petrinic, Comput. Mater. Sci. **136**, 20–28 (2017)
51. S. Plimpton, J. Comput. Phys. **117**, 1–19 (1995)
52. J. Chen, M.A. Tschopp, A.M. Dongare, J. Mater. Sci. **53**, 5745–5765 (2018)
53. Y. Ashkenazy, N. Pant, J. Zhou, P. Bellon, R.S. Averback, Acta Mater. **139**, 205–214 (2017)
54. G.P. PurjaPun, K.A. Darling, L.J. Kecskes, Y. Mishin, Acta Mater. **100**, 377–391 (2015)
55. M.P. Allen, D.J. Tildesley, *Computer Simulation of Liquids*, 2nd edn. (Oxford University Press, Oxford, 2017)
56. N. Gunkelmann, E.M. Bringa, K. Kang, G.J. Ackland, C.J. Ruestes, H.M. Urbassek, Phys. Rev. B **86**, 144111 (2012)
57. H. Sun, A. Kumar, C.V. Singh, Mater. Sci. Eng. A **761**, 138037 (2019)
58. Y. Ma, S. Zhang, Y. Xu, X. Liu, S.-N. Luo, Phys. Chem. Chem. Phys. **22**, 4741–4748 (2020)
59. A. Stukowski, Model. Simul. Mater. Sci. Eng. **18**, 015012 (2010)
60. A. Stukowski, K. Albe, Model. Simul. Mater. Sci. Eng. **18**, 085001 (2010)
61. P.M. Larsen, S. Schmidt, J. Schiøtz, Model. Simul. Mater. Sci. Eng. **24**, 055007 (2016)
62. C.S. Pande, K.P. Cooper, Prog. Mater Sci. **54**, 689–706 (2009)
63. A. Kardani, A. Montazeri, H.M. Urbassek, J. Mater. Sci. **57**, 16490–16506 (2022)
64. L. Zhu, X. Zheng, Acta Mech. **213**, 223–234 (2010)
65. P. Sharma, S. Ganti, J. Mater. Res. **18**, 1823–1826 (2003)
66. S.M. Foiles, Scr. Mater. **62**, 231–234 (2010)
67. H. Ke, I. Mastorakos, J. Mater. Res. **34**, 1093–1102 (2019)
68. R.F. Zhang, J. Wang, I.J. Beyerlein, T.C. Germann, Scr. Mater. **65**, 1022–1025 (2011)
69. R.G. Hoagland, J.P. Hirth, A. Misra, Philos. Mag. **86**, 3537–3558 (2006)
70. P. Heino, Comput. Mater. Sci. **20**, 157–167 (2001)
71. Y.Z. Tian, L.J. Zhao, S. Chen, A. Shibata, Z.F. Zhang, N. Tsuji, Sci. Rep. **5**, 16707 (2015)
72. V.V. Pogorelko, A.E. Mayer, Mater. Sci. Eng. A **642**, 351–359 (2015)
73. V.V. Dremov, P.V. Chirkov, A.V. Karavaev, Sci. Rep. **11**, 934 (2021)
74. G. Xi, J. Zhang, Y. Luo, J. Chen, H. Chen, Met. Mater. Int. (2022). https://doi.org/10.1007/s12540-022-01275-9
75. A. Rajput, S.K. Paul, Met. Mater. Int. **27**, 825–837 (2021)
76. F. Tan, F. Li, Q. Fang, J. Li, H. Feng, J. Mater. Sci. **56**, 9458–9469 (2021)
77. R.L. Morrison, S.J. Fensin, J.L.W. Carter, Materialia **7**, 100383 (2019)
78. X.J. Wu, A.K. Koul, Metall. Mater. Trans. A **26**, 905–914 (1995)